ACCSCIENCE PUBLISHING

International Journal of Bioprinting

RESEARCH ARTICLE

3D printing of aligned cellulose nanofiber hydrogels for enhanced AuNP-based SERS sensing

Tsui Yun Chung[1], Yu-Ting Lin[1], Priyanka Chaudhary[1], Hương Minh Trần[2], Wei-Fang Su[1,3], Meng-Fang Lin[1]*, and Yu-Ching Huang[1,4]*

[1]Department of Materials Engineering and Biochemical Technology R&D Center, Ming Chi University of Technology, New Taipei City, Taiwan

[2]Department of Chemical Engineering, School of Chemistry and Life Sciences, Hanoi University of Science and Technology, Hanoi, Vietnam

[3]Department of Materials Science and Engineering, National Taiwan University, Taipei City, Taiwan

[4]Department of Chemical and Materials Engineering, Chang Gung University, Taoyuan, Taiwan

Abstract

The development of flexible and 3D-printable surface-enhanced Raman scattering (SERS) substrates requires hydrogel architectures that support uniform nanoparticle distribution, structural robustness, and controlled filament formation. In this study, cellulose nanofibers (CNFs) and cellulose microfibers (CMFs) were incorporated into a poly(vinyl alcohol)/sodium alginate (PVA/SA) hydrogel crosslinked through borax to elucidate how fiber geometry, interfacial chemistry, and flow behavior collectively govern printability and plasmonic performance. CNFs form an interconnected and dynamically recoverable network that enhances viscosity, elastic recovery, and structural cohesion, enabling stable extrusion during 3D printing. The shear field within the printing nozzle further induces partial alignment of CNFs, generating more continuous microdomains that influence subsequent distribution of *in situ* grown gold nanoparticles (AuNPs). Spectroscopic and rheological analyses show that AuNP incorporation modulates local hydrogen bonding while preserving the dynamic borate crosslinking essential for filament fidelity. The 3D-printed CNF hydrogels exhibit clear and distinguishable SERS responses, with detectable rhodamine 6G (R6G) signals down to 10^{-6} M. This work provides a mechanistic understanding of how fiber morphology, flow-induced alignment, and nanoparticle-matrix interactions jointly define SERS behavior in printable hydrogels, offering a scalable design framework for next-generation soft-material sensing platforms.

Keywords: Cellulose nanofibers; Gold nanoparticles; 3D printing; Hydrogels; Surface-enhanced Raman scattering

***Corresponding authors:**
Meng-Fang Lin
(mflin@mail.mcut.edu.tw)
Yu-Ching Huang
(huangyc@mail.mcut.edu.tw)

Citation: Chung TY, Lin YT, Chaudhary P, *et al*. 3D printing of aligned cellulose nanofiber hydrogels for enhanced AuNP-based SERS sensing. *Int J Bioprint*. 2026:12(2):025010541.
doi: 10.36922/IJB025010541

Received: December 29, 2025

Revised: February 27, 2026

Accepted: March 9, 2026

Published online: April 23, 2026

1. Introduction

While surface-enhanced Raman spectroscopy (SERS) provides ultrasensitive molecular detection,[1-7] the practical deployment of conventional two-dimensional (2D) metallic films and colloidal assemblies is often constrained by nanoparticle aggregation, heterogeneous hot-spot formation, and temporal instability.[8,9] To address these issues, hydrogels have

emerged as promising alternatives. Their hydrated porous networks naturally confine metal nanoparticles in three dimensions, while polymers like poly(vinyl alcohol) (PVA) and various nanoparticle hybrids offer excellent structural adaptability and stability.[10–15] Beyond the fundamental interfacial chemistry between metal nanoparticles and hydrogel scaffolds,[16] recent progress has rapidly shifted toward three-dimensional (3D) printed plasmonic bioinks. These technologies allow for the construction of multiscale, programmable architectures capable of real-time volumetric SERS imaging and complex biomolecular detection.[17–19] However, most existing 3D-printed hydrogel SERS systems still rely on physically mixing nanoparticles within isotropic microstructures, which ultimately lacks directional plasmonic pathways. In particular, the ability to exploit flow-induced structural alignment during the extrusion process has remained largely unexplored.

Cellulose fibers (CFs) offer a compelling route toward microstructural control. Cellulose nanofibers (CNFs) and microfibers (CMFs) possess abundant hydroxyl/carboxyl groups capable of anchoring metal nanoparticles and exhibit fibrous morphologies that may influence crosslinking behavior and hydrogel mechanics.[20,21] Their high aspect ratio (CNFs) or larger diameter (CMFs) can potentially modulate network formation, plasmonic distribution, and mechanical resilience. Yet, the roles of fiber morphology and fiber–nanoparticle interfacial chemistry in shaping the plasmonic environment within hydrogels remain insufficiently understood. Extrusion-based 3D printing introduces an additional dimension of structural programmability. The shear field generated during extrusion can induce partial alignment of embedded fibers, enabling anisotropic architectures not achievable through bulk casting.[22,23] For SERS substrates, such alignment offers the potential to improve plasmonic uniformity and enhance hot-spot reproducibility by organizing nanoparticle-decorated fibers along preferred orientations. Despite this promise, the combined effects of nanoparticle–fiber interactions, fiber morphology, hydrogel viscoelasticity, and printing-induced alignment on SERS enhancement have rarely been elucidated.

In this study, we develop a 3D-printable AuNP/CF/PVA/SA hydrogel system that integrates *in situ* nanoparticle synthesis, nanoscale fiber reinforcement, and shear-mediated structural organization. Gold nanoparticles were grown directly on CNFs and CMFs to achieve controlled anchoring and dispersion, and the resulting hybrids were incorporated into borate-crosslinked PVA/SA hydrogels. The extrusion-based 3D printing process introduced shear-induced alignment, allowing the formation of architected hydrogel geometries. By correlating nanoparticle distribution, fiber-polymer interactions, rheological behavior, thermal stability, and SERS response, we establish how composite hydrogel architectures can be engineered to enhance signal uniformity and reproducibility. This integrated strategy demonstrates a manufacturable and structurally tunable framework for flexible SERS substrates, providing insights relevant to next-generation wearable and *in situ* analytical platforms.

2. Materials and methods

2.1. Materials

All chemicals were of analytical grade and used as received without further purification. Gold (III) chloride trihydrate ($HAuCl_4 \cdot 3H_2O$), sodium citrate ($Na_3Ct \cdot 2H_2O$), poly(vinyl alcohol) (PVA, 99+% hydrolyzed, Mw ≈ 89,000–98,000), sodium tetraborate (borax, AR grade), and rhodamine 6G (R6G) were purchased from Sigma-Aldrich (USA). Sodium tetraborate decahydrate was obtained from Fluka (USA). Alginic acid sodium salt (SA) was supplied by ACROS (Belgium). Carbonylated cellulose nanofibers (CNF) and carbonylated cellulose microfibers (CMF) were purchased from Qihong Technology Co., Ltd. (China). Ultrapure water (18.2 MΩ·cm) was used throughout the experiments.

2.2. Preparation of AuNPs/CNF and AuNPs/CMF

Two types of cellulose fibers with distinct sizes were used in this study: cellulose nanofibers (CNF) and cellulose microfibers (CMF). Gold nanoparticles were synthesized *in situ* on these fibers to obtain AuNPs/CNF and AuNPs/CMF, respectively. Both systems were prepared using identical precursor concentrations and reaction procedures based on a reported citrate-reduction method with modifications.[24] Carbonylated CNF powder was first diluted to obtain a 0.5 wt% CNF aqueous suspension, followed by ultrasonication to ensure complete dispersion. For AuNP loading, 50 mL of the CNF (or CMF) suspension was mixed with 2.5 mL of 5.0 mM $HAuCl_4 \cdot 3H_2O$ under vigorous stirring for 10 min. The pH of the mixture was adjusted to approximately 8 using NaOH. The reaction mixture was then heated to 90 °C in an oil bath with continuous stirring. Once the temperature stabilized, 0.5 mL of a 1 wt% sodium citrate solution was rapidly added to initiate the reduction reaction, which proceeded for 6 min. During the reaction, the color of the suspension gradually changed from pale yellow to gray-violet and eventually to bright red, indicating the formation of AuNPs on the fiber surfaces. After completion, the reaction was quenched by placing the suspension in an ice bath. The resulting AuNPs/CNF (or AuNPs/CMF) dispersions were stored at 4 °C in the dark until use.

2.3. Preparation of PVA/SA and fiber-reinforced hydrogels

Poly(vinyl alcohol) (PVA) was dissolved in deionized water at 90 °C under continuous stirring for approximately three hours until a clear solution was obtained. Sodium alginate (SA) was then added to prepare two polymer solutions containing either 8 wt% PVA with 1 wt% SA or 16 wt% PVA with 2 wt% SA, with all weight percentages defined relative to the total mass of the aqueous solution. The mixtures were stirred at room temperature for an additional four hours to ensure complete dissolution. Cellulose fibers of different sizes (CNF or CMF), as well as gold-nanoparticle-decorated cellulose (AuNPs/CNF or AuNPs/CMF), were subsequently incorporated into the PVA/SA solutions at volume ratios of 1:9, 1:3, and 1:1, forming precursor dispersions for CNF/PVA/SA or AuNPs/CNF/PVA/SA hydrogels. A 3.5 wt% borax solution, prepared separately at room temperature, was added (10 mL) to each precursor to trigger borate-mediated crosslinking. The mixtures were then held at 65 °C for one hour to allow sufficient network formation. After cooling to room temperature, the resulting hydrogels were stored for subsequent 3D printing and SERS analyses.

2.4. 3D printing of AuNPs/CNF/PVA/SA hydrogel

The AuNPs/CNF/PVA/SA hydrogel precursor was printed using a pneumatic extrusion-based 3D bioprinter (Allevi 2, Allevi Inc.). The printing models were designed using SOLIDWORKS software (Dassault Systèmes, France). Before printing, the hydrogel precursor was degassed by centrifugation at 4000 rpm for 20 min to remove entrapped air bubbles. The optimized printing parameters were as follows: air pressure of 44 psi, nozzle diameter of 0.52 mm, printing temperature of 65 °C, and printing speed of 6 mm/s. All samples were printed onto glass substrates and allowed to cool to room temperature to stabilize the printed architecture.

2.5. Structural and physicochemical characterization

UV-Vis spectra were recorded using a Jasco V-770 spectrophotometer. For AuNPs/CF composites, the wavelength range was set to 200–800 nm. For hydrogel transmittance measurements, the samples were placed between two quartz plates and compressed to a thickness of approximately 1.4 mm. The measurement wavelength range was set from 300 to 800 nm. A quartz sandwich without solvent was used as the baseline/reference. The functional groups of the AuNPs/CF composites and hydrogel samples were characterized by attenuated total reflection–Fourier transform infrared (ATR–FTIR) spectroscopy (PerkinElmer Spectrum Two) over a wavenumber range of 500–4000 cm^{-1} with a resolution of 4 cm^{-1}. The distribution of AuNPs on cellulose fibers was characterized by transmission electron microscopy (TEM) using a JEOL JEM-2100 LaB6 instrument. Thermogravimetric analysis (TGA) was conducted using a TA Instruments Q50 thermogravimetric analyzer. Measurements were carried out from 30 to 800 °C under an air atmosphere at a heating rate of 10 °C/min and a gas flow rate of 40 mL/min. Prior to TGA, the hydrogel specimens were freeze-dried for 24 hr using a laboratory freeze-dryer (HyperCOOL HC3110) to remove residual moisture. The micro-morphology of the AuNPs/CF composites samples were examined using field-emission scanning electron microscopy (FE-SEM; HITACHI S-5200). To observe the distribution of gold nanoparticles on cellulose fibers, the AuNPs/CF suspension was dropcast onto a glass substrate and allowed to dry prior to imaging. The dried samples were subsequently sputter-coated with a thin platinum (Pt) layer to improve conductivity before FE-SEM observation. This procedure enabled the visualization of the nanoparticle-decorated fibers.

2.6. Rheological characterization

Rheological measurements were conducted using a rotational rheometer (TA Instruments, HR20) equipped with 25 mm parallel plates, with the plate gap fixed at 0.1 mm for all tests. Frequency sweep experiments were performed at a constant strain of 0.5% over a range of 0.1–100 Hz to evaluate the frequency-dependent viscoelastic response. Amplitude sweep tests were carried out at a fixed frequency of 10 Hz while varying the strain amplitude from 0.1% to 100% to assess network integrity and yielding behavior. The storage modulus (G′), loss modulus (G″), and complex viscosity (|η*|) were recorded to characterize the elastic–viscous balance, crosslinking strength, and flow characteristics of the hydrogels.

2.7. Optical microscopy characterization

The alignment and birefringent behavior of the AuNPs/CFs/PVA/SA hydrogel within the 3D-printed scaffolds were examined using an optical microscope (Leica DM2500M, Leica Microsystems, Germany) equipped with cross-polarizers. Samples were placed on the microscope stage and carefully aligned with the optical axis to ensure uniform illumination across the field of view. Observations were conducted under both non-polarized and cross-polarized light conditions to evaluate structural anisotropy and orientation induced by the printing process. Images were captured at representative locations using appropriate objective lenses to ensure clear visualization of birefringence and alignment features. The presence of birefringence was taken as an indicator of anisotropic microstructural organization within the hydrogel matrix.

2.8. Performance evaluation of AuNPs/CNF/PVA/SA hydrogel SERS sensor

SERS measurements were performed using a confocal Raman microscope (Renishaw RL633) equipped with a 633 nm excitation laser operated at a power of 30 mW. Raman spectra were collected through a 50× objective lens with an acquisition time of 5 s. The optimized AuNPs/CFs/PVA/SA hydrogel sensor was printed into 1.0 × 1.0 cm^2 pieces before testing. Rhodamine 6G (R6G) aqueous solutions with various concentrations were used as probe molecules. A fixed volume of R6G solution was dropped onto the hydrogel substrates and incubated for 30 min to promote molecular adsorption and confinement within the hydrogel network. The samples were subsequently dried at 50 °C for 30 min prior to spectral acquisition. Unless otherwise specified, SERS measurements were performed at three independently selected locations for each sample to evaluate signal reproducibility. All spectra were collected under identical instrumental conditions to allow direct comparison of SERS performance among different hydrogel formulations.

3. Results and discussion

The *in situ* formation of Au nanoparticles (AuNPs) on cellulose fibers was examined to understand how fiber morphology influences nucleation behavior and nanoparticle distribution, as shown in Figure 1. FE-SEM images show that AuNPs formed on both CNF and CMF surfaces, but with distinct spatial arrangements. In the CNF-based samples (Figure 1b), AuNPs appear distributed along the nanofiber bundles, following their high-aspect-ratio geometry. For CMF (Figure 1c), the AuNPs tend to occupy the broader, micron-scale surface domains. These differences likely arise from the intrinsic structural characteristics of the two cellulose types, including their surface area and accessible functional groups, which

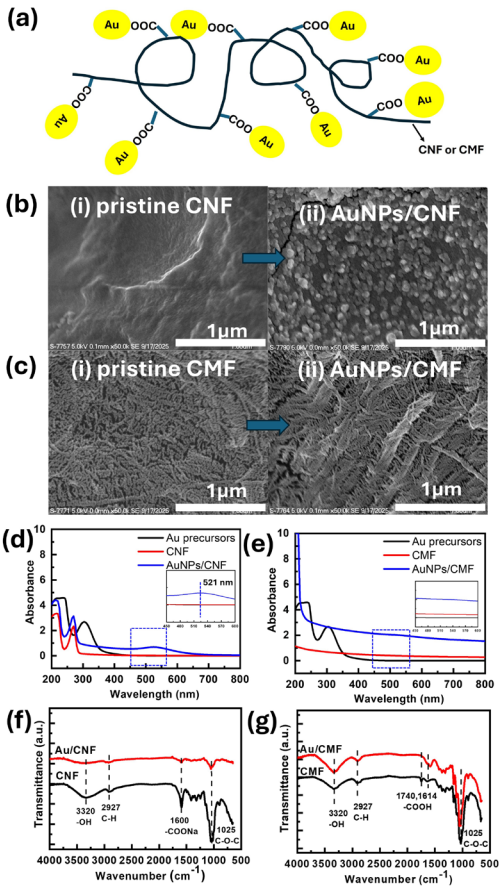

Figure 1. Schematic illustration of AuNPs integrated with CF and their effects on structure, distribution, and optical properties.(a) Schematic illustration of AuNPs incorporated with CNF and CMF. (b, c) FE-SEM images of pristine CNF (b-i), AuNPs/CNF (b-ii), pristine CMF (c-i), and AuNPs/CMF (c-ii). (d, e) UV–Vis absorption spectra of AuNPs/CNF (d) and AuNPs/CMF suspensions (e). (f, g) ATR–FTIR analysis of AuNPs/CNF (f) and AuNPs/CMF (g). Abbreviations: ATR: Attenuated total reflection; AuNPs: Gold nanoparticles; CMF: Cellulose microfibers; CNF: Cellulose nanofibers; FTIR: Fourier transform infrared spectroscopy.

influence nucleation density and attachment patterns. To verify nanoparticle formation on the fibers, transmission electron microscopy (TEM) and energy dispersive X-ray spectroscopy (EDS) were performed on the highly functionalized AuNPs/CNF samples (Figure S1). The high-resolution TEM micrographs (Figure S1b) clearly reveal the distinct spherical morphology and uniform distribution of the *in situ* grown AuNPs, supported by unequivocal elemental verification of Au (Figure S1c). UV-Vis absorption spectra further corroborate these morphological differences, as shown in Figure 1d,e. The AuNPs/CNF suspension displays a well-defined localized surface plasmon resonance (LSPR) peak at ~521 nm, consistent with discretely distributed, nanosized Au particles.[24] In contrast, the AuNPs/CMF system exhibits only a weak and broadened response in this region. This diminished optical response does not stem from a lower AuNP loading, but rather reflects a highly sparse distribution and localized nanoscale clustering. Figure 1f presents the attenuated total reflection–Fourier transform infrared spectroscopy (ATR–FTIR) analysis providing additional evidence of strong interfacial interactions between AuNPs and CNFs. Pristine CNF shows characteristic bands at 3320 cm^{-1} (O–H stretching), 1600 cm^{-1} (–COO^- stretching), 1025 cm-1 (C-O-C pyranose stretching), and 2927 cm^{-1} (C–H stretching), in agreement with previous reports on carboxylated CNFs.[25] After AuNP growth, these bands decrease in intensity, indicating that surface –OH and –COO^- groups participate in Au–O coordination or hydrogen bonding, thereby anchoring AuNPs and suppressing their migration and aggregation. In contrast, the FTIR spectra of CMF before and after Au deposition (Figure 1g) shows negligible changes in the O–H, C=O, and C–O–C bands,[26] confirming that the interfacial interaction between the agglomerated AuNPs and the CMF template is highly localized and strictly limited by the sparse availability of functional anchoring sites. These results establish that CNF and CMF each interact with AuNPs in systematically different ways due to their intrinsic structural and chemical characteristics. These distinctions provide a basis for understanding how fiber type influences subsequent network formation, rheological behavior, and ultimately SERS performance.

The incorporation of cellulose fibers into the PVA/SA-borate matrix led to distinct changes in the viscoelastic profiles depending on the fiber type and loading level. To verify the chemical interactions, the ATR–FTIR spectra of CNF/PVA/SA and CMF/PVA/SA hydrogels prepared with different fiber-to-polymer ratios (1:9, 1:3, 1:1), together with the spectra of pure fibers and the PVA/SA matrix, was analyzed as shown in Figure S2. In both CNF- and CMF-based systems, increasing the fiber content results in progressively enhanced O–H stretching near 3320 cm^{-1}, reflecting the greater availability of hydroxyl groups and the formation of more extensive hydrogen-bonding networks within the hydrogel. The carboxylate-associated peaks (1600 cm^{-1} for CNF samples; 1740 and 1614 cm^{-1} for CMF samples) become more pronounced as the fiber ratio increases, particularly in the CNF-containing samples, consistent with the higher surface functionalization and greater accessibility of CNF compared with CMF. Peaks near 1418 cm^{-1} (B–O–C) and 1041 cm^{-1} (C–O–C) correspond to skeletal vibrations, confirming successful crosslinking between borate ions and the polymer–fiber network.[27,28] Notably, the CNF and CMF series exhibit different degrees of spectral variation, which reflect differences in accessible surface groups and fiber morphology. These distinctions

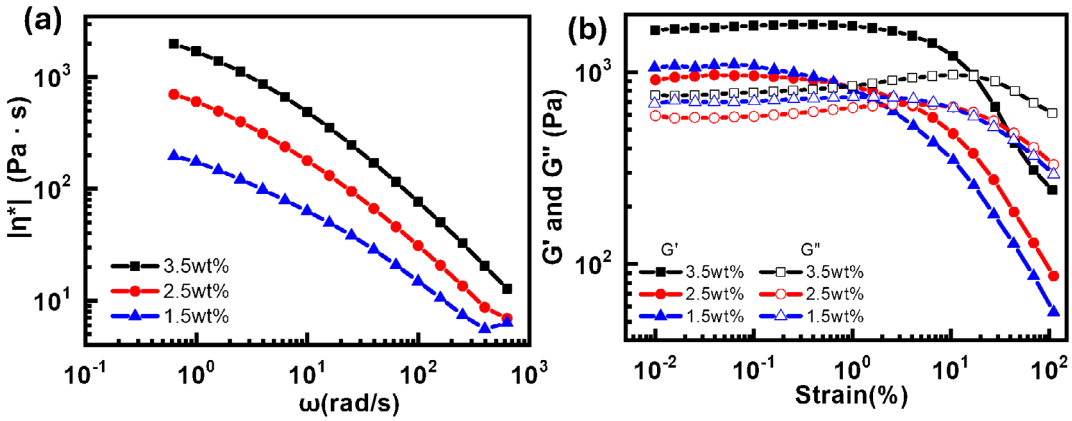

Figure 2. Rheological properties of PVA/SA hydrogels with different borax contents. (a) Complex viscosity ($|\eta^*|$) as a function of angular frequency, showing pronounced shear-thinning behavior. (b) Amplitude sweep profiles illustrating the linear viscoelastic region and the evolution of storage (G′) and loss (G″) moduli with increasing strain.
Abbreviations: PVA: Poly(vinyl alcohol); SA: Sodium alginate.

suggest that CNFs and CMFs modulate the polymer–fiber interactions in different ways within the hydrogel network.

The rheological characteristics of the PVA/SA–borax hydrogel were analyzed to identify the optimal crosslinking density required for stable extrusion and structural fidelity during 3D printing. The complex viscosity profiles, shown in Figure 2a, reveal pronounced shear-thinning behavior across all formulations, enabling the hydrogel to flow smoothly through the extrusion nozzle while maintaining structural stability upon deposition. Amplitude sweep results in Figure 2b indicate that each hydrogel preserves solid-like behavior (G′ > G″) within the linear viscoelastic region, confirming the formation of a dynamic borate-mediated crosslinked network. Increasing the borax concentration from 1.5 to 3.5 wt% leads to a progressive rise in storage modulus (G′) and yield stress, reflecting a denser di-diol–borate bonding network. However, when the borax content reaches 6 wt%, the excessive crosslinking stiffens the hydrogel to the point that extrusion becomes unstable and plug-flow behavior occurs, preventing continuous filament formation. At a borax concentration of 3.5 wt%, the hydrogel achieves an optimal balance of elasticity and flowability. The modulus is sufficiently high to support self-standing printed filaments, while the yield stress remains low enough to permit smooth, uninterrupted extrusion. The reversibility of the borate coordination bonds also facilitates rapid elastic recovery after high-strain deformation, a critical requirement for preserving line uniformity and interlayer adhesion. The 3.5 wt% formulation therefore provides the shear-dependent viscosity, rapid structural recovery, and mechanical stability required for reliable extrusion-based 3D printing. Furthermore, Figure S3 presents representative photographs of the 3D-printed hydrogels, verifying the macroscopic printing fidelity and illustrating the distinct visual changes before and after nanoparticle incorporation.

To elucidate how fiber loading influences the viscoelasticity and mechanical adaptability of the hybrid hydrogels, CNF or CMF were incorporated into the PVA/SA matrix at ratios of 1:9, 1:3, and 1:1 (fiber:PVA/SA), as presented in Figure 3. The viscosity–frequency curves (Figure 3a) reveal that all CNF formulations exhibit nearly identical shear-thinning profiles, indicating that increasing the CNF loading up to 1:1 does not significantly alter the bulk flow resistance. This suggests that the high aspect ratio of CNFs allows for efficient integration into the polymer network without causing excessive viscosity buildup. Furthermore, the amplitude sweep (Figure 3b) confirms that the 1:1 CNF hydrogel retains a high G′ comparable to the 1:9 formulation. This behavior is ideal, as it permits the incorporation of a high fiber content, crucial for maximizing SERS hotspot density, while strictly preserving the processability and structural fidelity of the hydrogel. In contrast, CMF-reinforced hydrogels exhibited a distinct response characterized by a monotonic increase in both complex viscosity and storage modulus with increasing fiber loading (Figure 3d,e). This trend is attributed to a macroscopic filler reinforcement effect, where the larger,

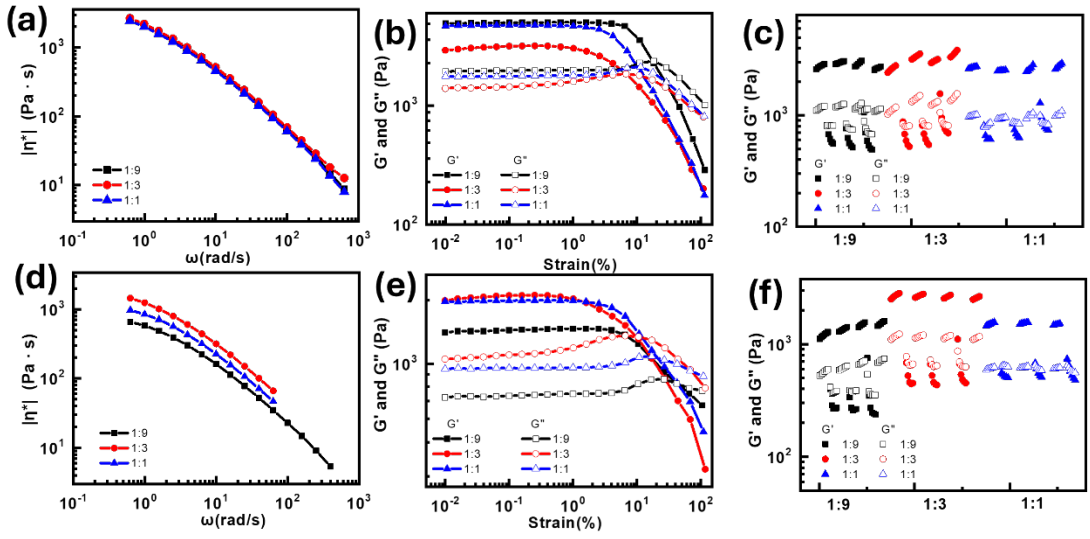

Figure 3. Rheological properties and thixotropic recovery of the cellulose/PVA/SA hydrogels with varying fiber loadings. The top row (a–c) corresponds to CNF/PVA/SA hydrogels, while the bottom row (d–f) corresponds to CMF/PVA/SA hydrogels. (a, d) Complex viscosity (|η*|) as a function of angular frequency, illustrating shear-thinning behavior. (b, e) Storage (G′) and loss (G″) moduli measured over a strain amplitude range of 0.01% to 100%. (c, f) Continuous step-strain oscillatory tests (alternating between 0.1% and 100% strain) to evaluate self-healing capability.
Abbreviations: CMF: Cellulose microfibers; CNF: Cellulose nanofibers; PVA: Poly(vinyl alcohol); SA: Sodium alginate.

rigid microfibers physically stiffen the matrix.

The self-healing capability of the hydrogels was further evaluated through alternating low-strain (0.1%) and high-strain (100%) oscillatory tests, as illustrated in Figure 3c,f. CNF-reinforced hydrogels with higher fiber loading (Figure 3c), particularly the 1:1 formulation, rapidly recover their initial storage modulus after repeated high-strain disruption. This rapid recovery is attributed to the dynamic borate–diol coordination and the CNF-mediated hydrogen-bonding network. In contrast, CMF-containing hydrogels exhibit incomplete structural restoration, with the G′ in the recovery phase failing to reach its initial magnitude (Figure 3f). This disparity suggests that the larger, rigid CMFs impose steric hindrance, disrupting the efficient reformation of the polymer matrix compared to the flexible nanofibrils. To visually corroborate this microstructural organization, polarized optical microscopy was employed to examine the hydrogel morphology,

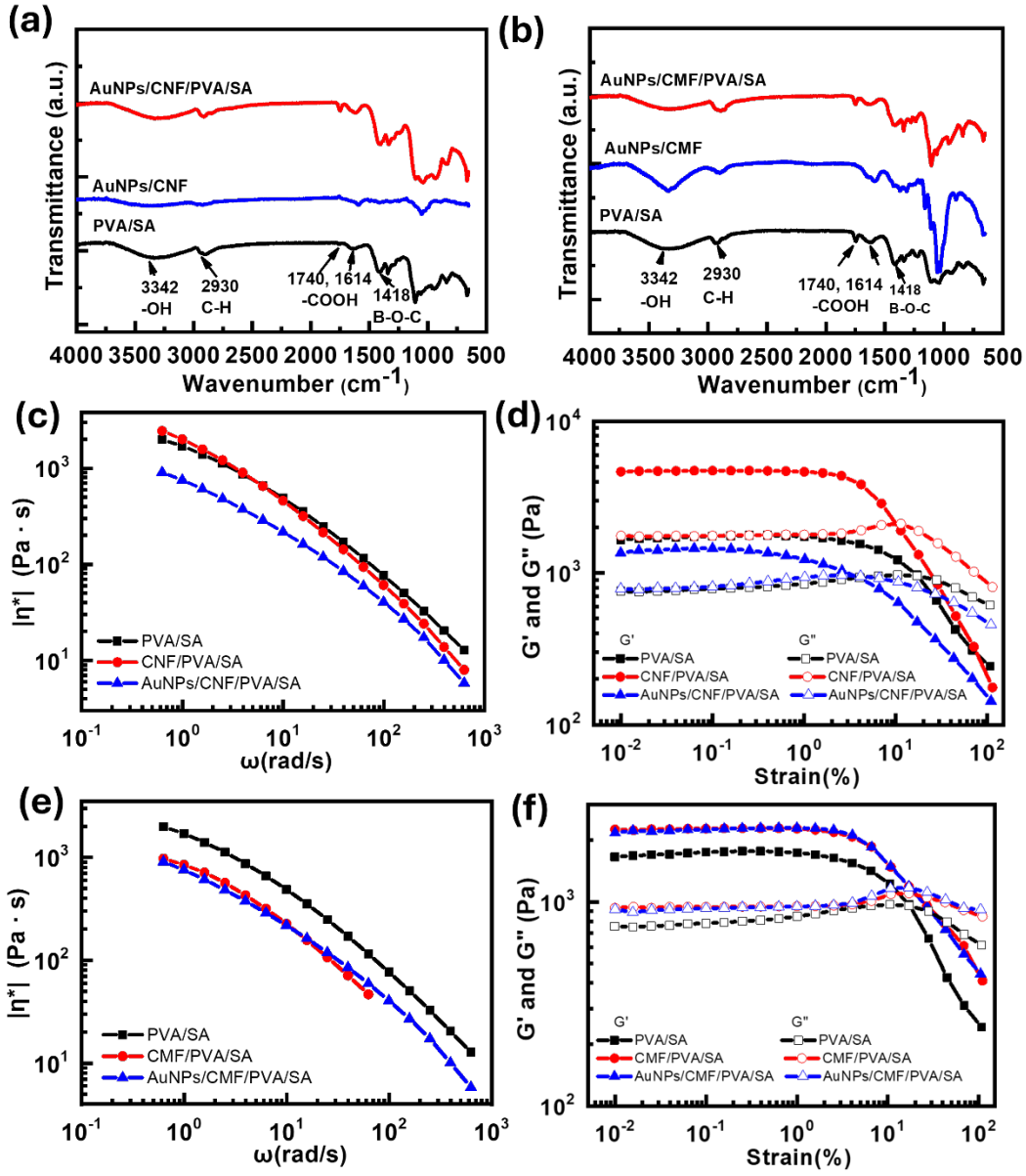

Figure 4. ATR–FTIR spectra and rheological behavior of AuNP-reinforced hydrogel systems. (a, b) FTIR spectra of AuNPs-loaded composites compared to pristine components for CNF-based and CMF-based systems, respectively. (c, e) Complex viscosity ($|\eta^*|$) as a function of angular frequency for CNF-based (c) and CMF-based hydrogels (e). (d, f) Amplitude sweep profiles for CNF-based (d) and CMF-based hydrogels (f).
Abbreviations: AuNPs: Gold nanoparticles; CMF: Cellulose microfibers; CNF: Cellulose nanofibers; PVA: Poly(vinyl alcohol); SA: Sodium alginate.

as shown in Figure S4. While solution-cast films show randomly distributed birefringent domains, the 3D-printed filaments exhibit pronounced, continuous interference colors running parallel to the printing direction. This distinct anisotropy confirms that the extrusion stress effectively orients the AuNP-decorated cellulose fibers along the flow axis. Based on these combined rheological and microstructural evidence, the CNF:PVA/SA ratio of 1:1 was selected for subsequent incorporation of AuNPs and for evaluating SERS performance.

The ATR–FTIR spectra were further analyzed to examine how the introduction of AuNPs alters the chemical environment within the fiber–hydrogel network. Figure 4a,b present the ATR–FTIR spectra of AuNPs/cellulose fibers, AuNPs/CF/PVA/SA, and the PVA/SA matrix. In both systems, the intensity of the broad O–H stretching band (~3342 cm^{-1}) decreases after AuNP incorporation, indicating that surface hydroxyl groups on cellulose fibers and PVA chains participate in coordination or adsorption onto the AuNP surfaces. This interaction partially consumes free –OH groups and disrupts the native hydrogen-bonding network. The carboxylate-associated absorptions at 1740 and 1614 cm^{-1} also diminish in the AuNP-containing samples, suggesting additional interactions between AuNPs and –COOH/–COO^- functionalities. These changes imply the formation of weak electrostatic associations or hydrogen bonding at the AuNP-fiber interface. Meanwhile, the characteristic B–O–C band at ~1418 cm^{-1} remains present across all hydrogels, confirming that borate crosslinking persists even after AuNPs incorporation and continues to stabilize the hydrogel network. The magnitude of these spectral alterations is significantly greater in the AuNPs/CNF series than in the AuNPs/CMF series, reflecting differences in the availability of functional groups and surface characteristics between the two fiber types. As a result, CNF provides an interfacial environment that supports more extensive AuNP attachment and a more uniform nanoparticle arrangement, features that can influence the development of local plasmonic fields within the hydrogel matrix. To connect these molecular-level interactions with macroscopic behavior, rheological tests were conducted on AuNP-reinforced hydrogels, as shown in Figure 4c–f. The viscosity–frequency curves (Figure 4c,e) show that AuNP incorporation slightly reduces the complex viscosity of both CNF- and CMF-based hydrogels while maintaining their characteristic shear-thinning behavior. This confirms that the AuNPs reorganize the surrounding fiber-polymer

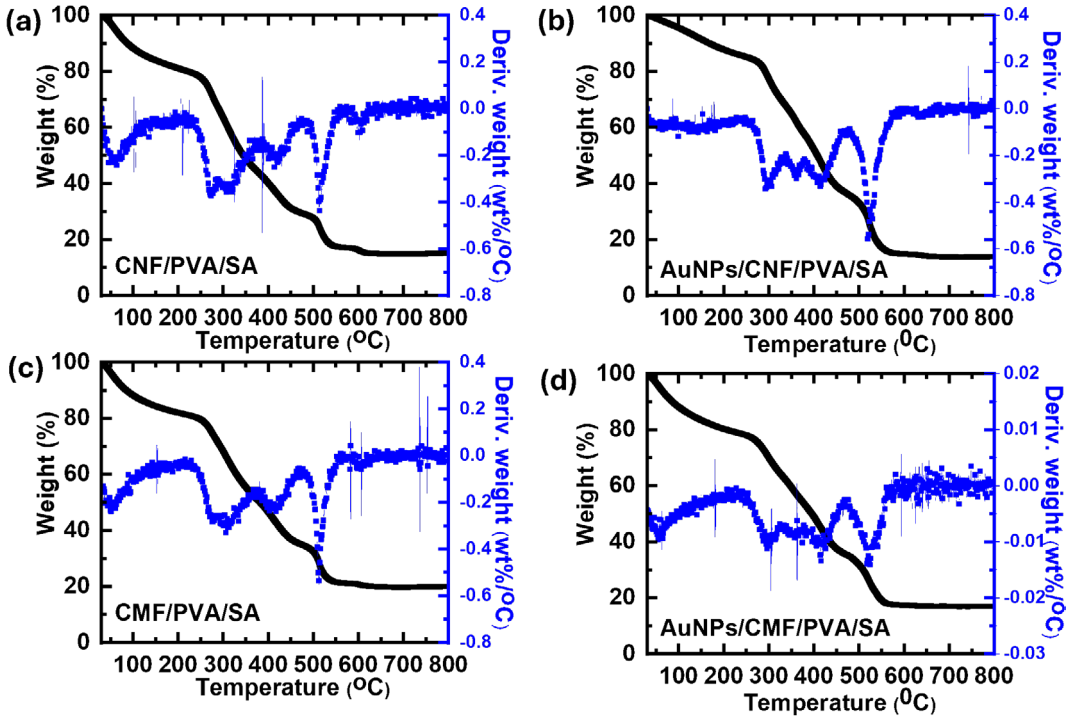

Figure 5. Thermal decomposition profiles of the cellulose fiber-reinforced hydrogels. (a) TGA (black lines, left axis) and DTG (blue lines, right axis) of CNF/PVA/SA, (b) AuNPs/CNF/PVA/SA, (c) CMF/PVA/SA, and (d) AuNPs/CMF/PVA/SA.

Abbreviations: AuNPs: Gold nanoparticles; CMF: Cellulose microfibers; CNF: Cellulose nanofibers; DTG: Derivative thermogravimetry; PVA: Poly(vinyl alcohol); SA: Sodium alginate; TGA: Thermogravimetric analysis.

network without compromising structural integrity required for extrusion. Figure S3 demonstrates that both pristine and AuNP-loaded hydrogels are printable, as they can be smoothly extruded through the printing nozzle and retain sufficient structural integrity to form self-supporting 3D architectures. Furthermore, oscillatory amplitude sweeps, as shown in Figure 4d,f, reveal that the G′ and G″ remain comparable to those of the pristine hydrogel within the linear viscoelastic region (LVR). This suggests that the dynamic borate-crosslinked network continues to function effectively after AuNP addition, providing sufficient mechanical strength to support the 3D-printed structure. Overall, these results confirm that AuNP incorporation subtly modifies, yet does not disrupt, the viscoelastic behavior of the hydrogels, thereby preserving the flowability, structural resilience essential for reliable extrusion-based 3D printing.

Figures 5 and S5 illustrate the TGA and DTG curves of the hydrogel composites. Both CNF- and CMF-based matrices exhibit a characteristic multi-stage decomposition pattern, initiated by moisture evaporation (<150 °C) and followed by the major pyrolysis of the PVA/SA backbone and cellulose components (200–400 °C).[23] An additional weight-loss event is observed near 550 °C, which is attributed to the oxidative combustion of carbonaceous residues under an air atmosphere. The char residue analysis after pyrolysis at 700 °C reveals that the pristine hydrogel without AuNP incorporation exhibits a slightly higher residual mass than the AuNPs/CNF hydrogel. The reduced residual mass observed in the AuNP-loaded hydrogels under an oxidative atmosphere can be attributed to the catalytic oxidation effect of AuNPs, which promotes the combustion of carbonaceous residues, outweighing the minor mass contribution of metallic nanoparticles. Because this catalytic effect obfuscates direct quantification via TGA, comparable gold loading was ensured through the strictly controlled *in situ* synthesis protocol. Specifically, identical concentrations and volumes of gold precursors were utilized for both cellulose templates, guaranteeing that the macroscopic Au loading is highly comparable between the CNF and CMF systems. Thus, the superior SERS activity of the CNF hydrogels is intrinsically linked to the extrusion-induced structural alignment and uniform hot-spot distribution, rather than variations in total gold content.

Measuring the optical transmittance is essential for SERS hydrogels, as sufficient light penetration is required to effectively excite embedded plasmonic nanoparticles and generate strong Raman enhancement. Figure 6 presents the optical transmittance of the hydrogels, revealing that the pristine hydrogel maintains near-complete transparency. The incorporation of AuNPs leads to a pronounced reduction in transmittance, particularly at around 520 nm, corresponding to the characteristic LSPR absorption of Au nanoparticles. Notably, the AuNPs/CNF/PVA/SA hydrogel exhibits lower transmittance than the AuNPs/CMF/PVA/SA system, suggesting a higher effective dispersion and stronger plasmonic interaction within the CNF network. Consequently, these structural and optical characteristics facilitate optimized light–nanoparticle interactions and maximize localized electromagnetic field enhancement, thereby establishing a superior foundation for plasmonic activity and SERS performance.

Supported by the structural alignment and thermal stability confirmed above, the SERS responses obtained from the AuNP-loaded hydrogels highlight the critical role

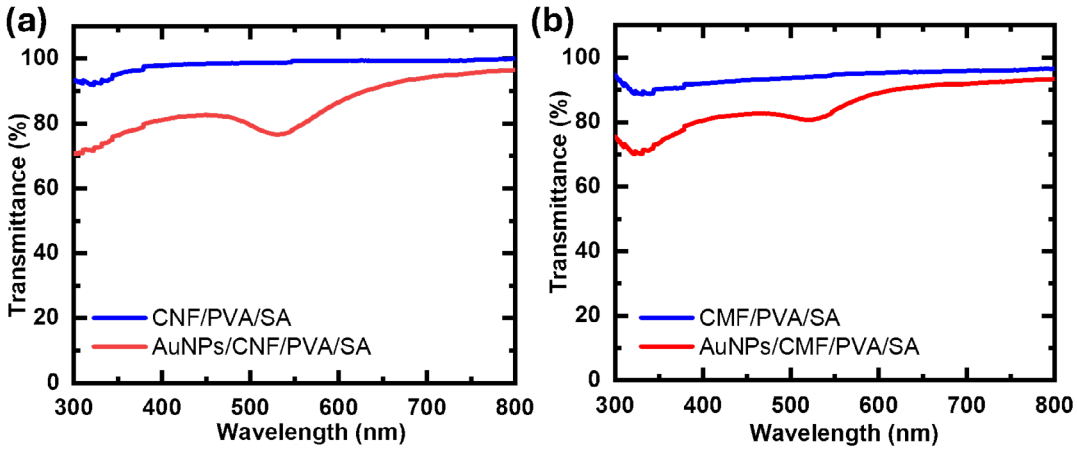

Figure 6. Comparative UV–Vis transmittance spectra showing the effect of AuNP incorporation: (a) CNF-based hydrogels and (b) CMF-based hydrogels. The black curves correspond to pristine hydrogels, while the red curves represent the AuNP-loaded composites.
Abbreviations: AuNPs: Gold nanoparticles; CMF: Cellulose microfibers; CNF: Cellulose nanofibers; PVA: Poly(vinyl alcohol); SA: Sodium alginate.

of extrusion-induced structural alignment in governing plasmonic activity. Compared with cast hydrogels, the 3D-printed CNF/PVA/SA structures exhibit directionally organized nanofiber networks that arise as high-aspect-ratio CNFs align along the shear field during extrusion. This anisotropic arrangement promotes tighter AuNP confinement, reduced interparticle spacing, and more continuous electromagnetic hot-spot pathways, resulting in the markedly stronger Raman intensities observed in Figure 7a for the characteristic R6G vibrational modes. Cast CNF hydrogels, in contrast, display a more isotropic microstructure, leading to a less interconnected AuNP distribution and correspondingly weaker enhancement. The concentration-dependent measurements further demonstrate the importance of printing-induced alignment. As shown in Figure 7b, prominent SERS features, particularly at 1363 and 1508 cm^{-1}, remain discernable down to 10^{-6} M R6G in the printed CNF hydrogels, reflecting the ability of the aligned nanofiber scaffold to sustain a dense and stable hot-spot environment even at ultra-low analyte concentrations. The continuity of the anisotropic CNF network supports plasmonic coupling over longer length scales, thereby preserving signal intensity throughout the detection range. CMF-based hydrogels, whether printed or cast, do not exhibit comparable alignment due to the larger fiber diameter and lower aspect ratio of CMF, which limit their ability to reorganize under extrusion. As a result, the AuNP distribution remains relatively isotropic, producing weaker SERS signals and a much higher detection threshold (only visible at $\geq 10^{-3}$ M), consistent with the spectra shown in Figure 7c. These observations underscore that fiber geometry governs the extent to which printing can induce mesoscale alignment, thereby influencing hot-spot formation efficiency.

Crucially, it is important to note that the SERS measurements in this study were conducted on dried hydrogel specimens. During the analyte loading process, the as-printed hydrogels were susceptible to structural degradation in the mildly acidic R6G solution due to the pH-sensitive dissociation of the dynamic borate–diol coordination bonds.[27] Consequently, a combination of freeze–thawing and controlled oven heating was employed to physically stabilize the network and preserve structural integrity. While this drying process successfully prevented network collapse, it inevitably induced volume shrinkage. This dehydration-induced densification reduces the

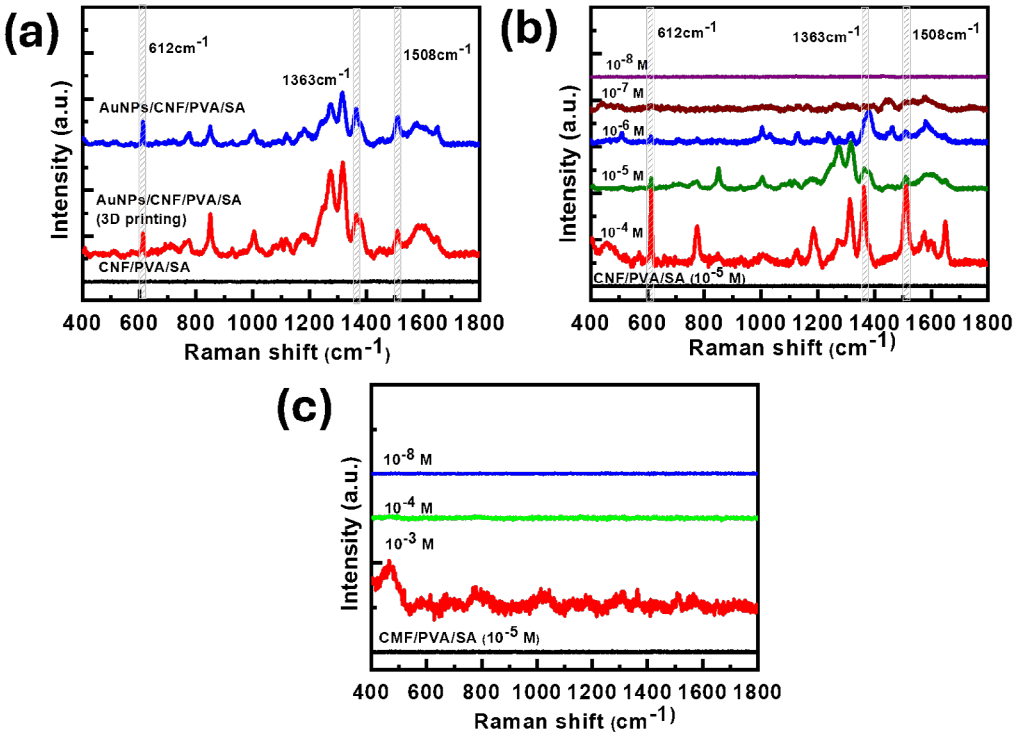

Figure 7. SERS performance using R6G as the probe. (a) Comparison of pristine, cast, and 3D-printed CNF-based hydrogels at 10^{-5} M. (b) Concentration-dependent spectra of 3D-printed AuNPs/CNF hydrogels (10^{-4}–10^{-8} M) versus a pristine control. (c) SERS spectra of AuNPs/CMF hydrogels at varying concentrations (10^{-3}–10^{-8} M).

Abbreviations: AuNPs: Gold nanoparticles; CMF: Cellulose microfibers; CNF: Cellulose nanofibers; PVA: Poly(vinyl alcohol); SA: Sodium alginate; SERS: Surface-enhanced Raman scattering.

interparticle distances between the embedded AuNPs, altering the plasmonic coupling and generating denser electromagnetic hotspots compared to a swollen state. Therefore, the SERS performance observed herein reflects a structurally concentrated plasmonic network, and direct comparisons with fully hydrated hydrogel systems should be treated with this fundamental structural distinction. Table S1 compares the SERS performance of our AuNPs/CNF/PVA/SA hydrogel with other recently reported flexible and polymer-based SERS systems. The developed platform achieves a reliable detection limit of 10^{-6} M, placing it well within the performance range of current state-of-the-art flexible substrates. Beyond sensitivity, our hydrogel system addresses several practical limitations of conventional 2D flexible SERS platforms (such as metallic-coated PDMS or PET films), which typically lack structural programmability and dynamic adaptability. At the microscale, combining CNF reinforcement with extrusion-driven alignment effectively creates a dense and uniform hot-spot network. At the macroscale, the formulation is readily compatible with scalable printing processes. Furthermore, integrating 3D printability with dynamic self-healing provides significant practical benefits. The self-healing network can recover from external mechanical stress to sustain long-term durability, while the extrusion process ensures precise control over the architecture of the substrates. These features make this platform a highly adaptable and practical candidate for future wearable sensing applications.

4. Conclusion

This work demonstrates a systematic framework for designing printable hydrogel-based SERS substrates by integrating fiber morphology, dynamic crosslinking chemistry, and extrusion-induced structural organization. CNF and CMF were employed to disentangle the effects of fiber geometry on network formation, mechanical adaptability, and interfacial interactions with *in situ* grown AuNPs. CNFs form a highly interconnected network with rapid elastic recovery, enabling stable extrusion and partial fiber alignment under the shear field generated within the printing nozzle. This alignment produces more continuous fiber microdomains that influence AuNP distribution within the hydrogel matrix. Spectroscopic and rheological analyses reveal that AuNP incorporation modulates hydrogen-bonding interactions without disrupting the dynamic borate crosslinking essential for printability. The reinforced hydrogels retain their viscoelastic integrity and shear-thinning characteristics after deformation, ensuring structural fidelity during layer-by-layer deposition. Thermal analysis further confirms that the fiber-reinforced frameworks maintain stability during processing, providing a reliable foundation for plasmonic functionality. SERS measurements show that the 3D-printed hydrogels provide consistent signal enhancement, with CNF-based systems achieving reproducible spectral responses at concentrations as low as 10^{-6} M R6G. These findings establish that the interplay between fiber geometry, shear-induced organization, and nanoparticle-matrix interactions govern the sensing performance of soft, printable SERS materials. The integrated design strategy presented here offers a promising route toward flexible, architecturally tunable, and scalable hydrogel-based sensing platforms suitable for next-generation chemical and biological detection.

Acknowledgments

None.

Funding

This research was supported by the National Science and Technology Council (NSTC) of Taiwan under Grant No. NSTC 114-2221-E-131-012-MY3, 114-2221-E-131-038, and 112-2628-E-131-001-MY4. The funder had no role in the study design, data collection and analysis, decision to publish, or preparation of the manuscript.

Conflict of interest

The authors declare they have no competing interests.

Author contributions

Conceptualization: Meng-Fang Lin, Yu-Ching Huang
Formal analysis: Tsui-Yun Chung, Yu-Ting Lin
Funding acquisition: Meng-Fang Lin, Yu-Ching Huang
Investigation: Tsui-Yun Chung, Yu-Ting Lin, Priyanka Chaudhary, Hương Minh Trần
Methodology: Tsui-Yun Chung, Yu-Ting Lin
Resources: Meng-Fang Lin, Yu-Ching Huang
Supervision: Wei-Fang Su, Meng-Fang Lin, Yu-Ching Huang
Writing–original draft: Tsui-Yun Chung
Writing–review & editing: Meng-Fang Lin, Yu-Ching Huang

Ethics approval and consent to participate

Not applicable.

Consent for publication

Not applicable.

Availability of data

The datasets generated and/or analyzed during the current study are available from the corresponding author upon reasonable request.

References

1. Zong C, Xu M, Xu LJ, *et al*. Surface-Enhanced Raman Spectroscopy for Bioanalysis: Reliability and Challenges. *Chem Rev*. 2018;118(10):4946-4980.

   doi: 10.1021/acs.chemrev.7b00668

2. Sinha SS, Jones S, Pramanik A, Ray PC. Nanoarchitecture Based SERS for Biomolecular Fingerprinting and Label-Free Disease Markers Diagnosis. *Acc Chem Res*. 2016;49(12):2725-2735.

   doi: 10.1021/acs.accounts.6b00384

3. Wu C, Li F, Lv F, Yao P, Bi M, Xue T. Fabrication of hydrogels with nanoparticles as surface-enhanced Raman scattered (SERS) substrates and their application in Raman imaging. *Mater Res Express*. 2021;8(1):015008.

   doi: 10.1088/2053-1591/abd5d0

4. Dallari C, Lenci E, Trabocchi A, *et al*. Multilayered bioorthogonal SERS nanoprobes selectively aggregating in human fluids: a smart optical assay for β-amyloid peptide quantification. *ACS Sens*. 2023;8(10):3693-3700.

   doi: 10.1021/acssensors.3c00225

5. Kant K, Beeram R, Cao Y, *et al*. Plasmonic nanoparticle sensors: current progress, challenges, and future prospects. *Nanoscale Horiz*. 2024;9:2085-2166.

   doi: 10.1039/D4NH00226A

6. Wu J, Zhou X, Li P, *et al*. Ultrasensitive and simultaneous SERS detection of multiplex microRNA using fractal gold nanotags for early diagnosis and prognosis of hepatocellular carcinoma. *Anal Chem*. 2021;93(25):8799-8809.

   doi: 10.1021/acs.analchem.1c00478

7. Joseph MM, Narayanan N, Nair JB, *et al*. Exploring the margins of SERS in practical domain: an emerging diagnostic modality for modern biomedical applications. *Biomaterials*. 2018;181:140-181.

   doi: 10.1016/j.biomaterials.2018.07.045

8. Xu J, Du J, Jing C, Zhang Y, Cui J. Facile Detection of Polycyclic Aromatic Hydrocarbons by a Surface-Enhanced Raman Scattering Sensor Based on the Au Coffee Ring Effect. *ACS Appl Mater Interfaces*. 2014;6(9):6891-6897.

   doi: 10.1021/am500705a

9. Liu Z, Su R, Xiao X, Li G. Boronic acid ester-based hydrogel as surface-enhanced Raman scattering substrates for separation, enrichment, hydrolysis and detection of hydrogen peroxide residue in dairy product all-in-one. *Talanta*. 2025;281:126900.

   doi: 10.1016/j.talanta.2024.126900

10. Wang H, Xu P, Chen Y, *et al*. "Partner" cellulose gel with "dialysis" function: Achieve the integration of filtration-enrichment-SERS detection. *Biosens Bioelectron*. 2025;267:116775.

    doi: 10.1016/j.bios.2024.116775

11. Zhang J, Wang Y, Wei Q, *et al*. A 3D printable, highly stretchable, self-healing hydrogel-based sensor based on polyvinyl alcohol/sodium tetraborate/sodium alginate for human motion monitoring. *Int J Biol Macromol*. 2022;219:1216-1226.

    doi: 10.1016/j.ijbiomac.2022.08.175

12. Zhang H, Fu C, Yong LC, Sun N, Liu FG. Flexible and Transparent PVA/CNF Hydrogel with Ultrahigh Dielectric Constant. *ACS Appl Polym Mater*. 2024;6(10):5706-5713.

    doi: 10.1021/acsapm.4c00302

13. Chen M, Zhang J, Zhu X, *et al*. Hybridizing Silver Nanoparticles in Hydrogel for High-Performance Flexible SERS Chips. *ACS Appl Mater Interfaces*. 2022;14(22):26216-26224.

    doi: 10.1021/acsami.2c04087

14. Zhang B, Yang J, Jiang Q, *et al*. AuNPs/C-CNF/PVA hydrogel SERS sensor for comprehensive detection of antitumor drug separation and enrichment. *Chem Eng J*. 2025;516:164282.

    doi: 10.1016/j.cej.2025.164282

15. Ling H, Zhao Z, Zhang Z, Chen S, Maimaiti Z. PVA/AgNP hydrogel SERS substrate combined with machine learning for highly sensitive detection of organic selenium species. *Anal Methods*. 2026.

    doi: 10.1039/D5AY02045J

16. Ma T, Lv L, Ouyang C, *et al*. Rheological behavior and particle alignment of cellulose nanocrystal and its composite hydrogels during 3D printing. *Carbohydrate Polymers*. 2021;253:117217.

    doi: 10.1016/j.carbpol.2020.117217

17. Troncoso-Afonso L, Henríquez-Banegas YM, Vinnacombe-Willson GA, *et al*. Using thiol–ene click chemistry to engineer 3D printed plasmonic hydrogel scaffolds for SERS biosensing. *Biomater Sci*. 2025;13(11):2936-2950.

    doi: 10.1039/D4BM01529K

18. Wang W, Vikesland PJ. SERS-Active Printable Hydrogel for 3D Cell Culture and Imaging. *Anal Chem*. 2023;95(49):18055-18064.

    doi: 10.1021/acs.analchem.3c02641

19. Ventisette I, Mattii F, Dallari C, *et al*. Gold-Hydrogel Nanocomposites for High-Resolution Laser-Based 3D Printing of Scaffolds with SERS-Sensing Properties. *ACS Appl Bio Mater*. 2024;7(7):4497-4509.

    doi: 10.1021/acsabm.4c00379

20. Heggset EB, Strand BL, Sundby KW, Simon S, Chinga-Carrasco G, Syverud K. Viscoelastic properties of nanocellulose based inks for 3D printing and mechanical properties of CNF/alginate biocomposite gels. *Cellulose*. 2018;26(1):581-595.

    doi: 10.1007/s10570-018-2142-3

21. Li M, Wang Y, Wei Q, Zhang J, Chen X, An Y. A High-Stretching, Rapid-Self-Healing, and Printable Composite Hydrogel Based on Poly(Vinyl Alcohol), Nanocellulose, and Sodium Alginate. *Gels*. 2024;10(4):258.

doi: 10.3390/gels10040258

22. Li Y, Zhu H, Wang Y, *et al*. Cellulose-Nanofiber-Enabled 3D Printing of a Carbon-Nanotube Microfiber Network. *Small Methods*. 2017;1(10):1700222.

doi: 10.1002/smtd.201700222

23. Almohammed S, Alruwaili M, Reynaud EG, Redmond G, Rice JH, Rodriguez BJ. 3D-Printed Peptide-Hydrogel Nanoparticle Composites for Surface-Enhanced Raman Spectroscopy Sensing. *ACS Appl Nano Mater*. 2019;2(8):5029-5034.

doi: 10.1021/acsanm.9b00940

24. He H, Chen R, Zhang L, Shen W. Growth of gold nanoparticles on cellulose nanofibers. *Cellulose*. 2020;27(9):5041-5053.

doi: 10.1007/s10570-020-03142-5

25. Yang Y, Li D, Yan N, Guo F. A new 3D printing strategy by enhancing shear-induced alignment of gelled nanomaterial inks resulting in stronger and ductile cellulose films. *Carbohydr Polym*. 2024;340:122269.

doi: 10.1016/j.carbpol.2024.122269

26. Lal SS, Mhaske ST. AgBr and AgCl nanoparticle doped TEMPO-oxidized microfiber cellulose as a starting material for antimicrobial filter. *Carbohydr Polym*. 2018;191:266-279.

doi: 10.1016/j.carbpol.2018.03.011

27. Lu B, Lin F, Jiang X, *et al*. One-Pot Assembly of Microfibrillated Cellulose Reinforced PVA–Borax Hydrogels with Self-Healing and pH-Responsive Properties. *ACS Sustain Chem Eng*. 2016;5(1):948-956.

doi: 10.1021/acssuschemeng.6b02279

28. Xu K, Wang Y, Zhang B, Zhang C, Liu T. Stretchable and self-healing polyvinyl alcohol/cellulose nanofiber nanocomposite hydrogels for strain sensors with high sensitivity and linearity. *Compos Commun*. 2021;24:100677.

doi: 10.1016/j.coco.2021.100677